Crystal Structure, Magnetic Properties, and Ionic Conductivity of a New Mixed-Anion Phosphate $Na_4Ni_5(PO_4)_2(P_2O_7)_2$

Francisca Sanz,[‡] Carmen Parada,[†] Jose M. Rojo,[‡] and Caridad Ruiz-Valero*[,‡]

Instituto de Ciencia de Materiales de Madrid, CSIC, Cantoblanco, E−28049 Madrid, Spain, and Departamento de Química Inorgánica, Facultad de Ciencias Químicas, Universidad Complutense, E−28040 Madrid, Spain

Received December 2, 1998. Revised Manuscript Received April 12, 1999

Single crystals of the new sodium phosphate $Na_4Ni_5(PO_4)_2(P_2O_7)_2$ have been isolated and their structure has been determined by X-ray diffraction techniques. This compound crystallizes in the monoclinic space group $P2_1/c$ with $a = 12.544(2)$ Å, $b = 6.596(1)$ Å, $c = 10.572(2)$ Å, $\beta = 103.731(3)°$, and $Z = 2$. Its three-dimensional structure can be described as formed by $(Ni_5P_2O_{22})_\infty$ infinite blocks parallel to the *bc* plane being the interblock linkages via P−O−P bridges of the diphosphate groups. There are tunnels along the [100] direction, crossing the $(Ni_5P_2O_{22})_\infty$ blocks, which host the sodium cations. The framework is built up from PO_4 tetrahedra, P_2O_7 groups, NiO_6 octahedra, and Ni_2O_9 units formed by face-sharing between two NiO_6, which is unusual in these kinds of compounds. Magnetic measurements reveal the presence of antiferromagnetic interactions in the Ni^{2+} sublattice, at about 8 K. The ionic conductivity, due to the motion of sodium ions, was measured at different temperatures (300−700 °C) in the frequency range $1-10^5$ Hz. The determined activation energy was 0.99 eV and the conductivity at 500 °C was 2.8×10^{-6} S cm^{-1}.

Introduction

In the search for new compounds with high ionic conductivity or good catalytic properties, many phases in the system A−M−P−O (A = monovalent metal, M = transition metal) have been synthesized. The phosphorus, oxygen, and M atoms are linked by rather covalent bonds and tend to form two- or three-dimensional frameworks, while the A cations are joined by essentially ionic forces.[1−9] Among these compounds, only few contain both phosphate and diphosphate groups.[10−15] We have recently reported the structure of one of them, $Na_4Co_3(PO_4)_2(P_2O_7)$, built up from corner- and edge-sharing between MO_6 octahedra, PO_4, and P_2O_7 groups, giving rise to a polyhedral connectivity which leads to a three-dimensional channel network, where the sodium cations are located.[16]

The present paper deals with a new mixed anion compound, $Na_4Ni_5(PO_4)_2(P_2O_7)_2$, in which there are confacial octahedral Ni_2O_9 units, rarely observed to date. The magnetic properties and the ionic conductivity have also been investigated in this new material.

Experimental Section

Synthesis. Crystals of $Na_4Ni_5(PO_4)_2(P_2O_7)_2$ were grown by melting a mixture of $Na_4P_2O_7$ (98%) and α-$Ni_2P_2O_7$ in the molar ratio Na/Ni = 1:2. Since α-$Ni_2P_2O_7$ is not a commercial reactant, it was previously synthesized from $Ni(NO_3)_2 \cdot 6H_2O$ (99.999%) and $NH_4H_2PO_4$ (99.999%). These reagents were well mixed in an agate mortar in equimolar ratio and heated at 300 °C. Later, the amorphous solid was reground and heated at 600 °C during 3 days. After these treatments, the X-ray diffraction pattern of the well-crystallized yellow solid coincided with that of α-$Ni_2P_2O_7$ (powder diffraction file 39-0710).[17]

The obtained α-$Ni_2P_2O_7$ and $Na_4P_2O_7$ were held in a porcelain crucible in molar ratio 2:1 and slowly heated to 900 °C, the melting temperature. The furnace was kept at this temperature for 2 h to homogenize the melt, being then slowly cooled to 400 °C at a rate of 10 °C/h and finally quenched to room temperature.

* To whom correspondence should be addressed. Telephone: +34 91 3349026. Fax: +34 91 3720623. e-mail: caridad@immrx1.icmm.csic.es.

[†] Universidad Complutense.

[‡] Instituto de Ciencia de Materiales de Madrid.

(1) Barj, M.; Lucazeau, G.; Delmas, C. *J. Solid State Chem.* **1992**, *100*, 14.

(2) Alamo, J. *Solid State Ionics* **1993**, *547*, 65.

(3) Clearfield, A. *Chem. Rev.* **1991**, *88*, 125.

(4) Villenueve, G.; Suh, K. S.; Amorós, P.; Casán-Pastor, N.; Beltran, D. *Chem. Mater.* **1992**, *4*, 108.

(5) Kasthuri Rangsn, K.; Gopdakrishnan, J. *Inorg. Chem. Mater.* **1992**, *4*, 1969.

(6) Miguel, P. F.; Borddes, E.; Katz, J. L. *J. Solid State Chem.* **1996**, *124*, 95.

(7) Feng, P.; Bu, X.; Tolbert, S. H.; Stucky, G. D. *J. Am. Chem. Soc.* **1997**, *119*, 2497.

(8) Wilkinson, A. P. *Inorg. Chem.* **1997**, *36*, 1602.

(9) Chen, J.; Jones, R. H.; Natarajan, S.; Hursthouse, M. B.; Thomas, J. M. *Angew. Chem., Int. Ed. Engl.* **1994**, *36*, 369.

(10) De la Rochère, M.; Kahn, A.; D'Yvoire, F.; Bretey, E. *Mater. Res. Bull.* **1985**, *20*, 27.

(11) Lii, K. H.; Wen, N. S.; Su, C. C.; Chueh, B. R. *Inorg. Chem.* **1992**, *31*, 439.

(12) Haushalter, R. C. *J. Solid State Chem.* **1990**, *89*, 215.

(13) Lii, K. H.; Wen, N. S.; Su, C. C.; Chueh, B. R. *Inorg. Chem.* **1992**, *31*, 439.

(14) Dvoncova, E.; Lii, K.-H.; Li, C.-H.; Chen, T.-M. *J. Solid State Chem.* **1993**, *106*, 485.

(15) Grandin, A.; Leclaire, A.; Borel M. M.; Raveau; B. *J. Solid State Chem.* **1995**, *115*, 52.

(16) Sanz, F.; Parada, C.; Amador, U.; Monge, M. A.; Ruiz-Valero, C. *J. Solid State Chem.* **1996**, *123*, 129.

(17) ICPDS International Centre for Diffraction Data 1986, 1601 Park Line, Swarthmore, PA 19081.

10.1021/cm981105s CCC: $18.00
Published on Web 09/18/1999

Two kind of crystals were extracted from the resulting product. One of them, brown in color, was identified as $Na_4Ni_7(PO_4)_6$, whose structure was previously determined.[18] The other, yellow in color, has the composition $Na_4Ni_5(PO_4)_2(P_2O_7)_2$ and constitutes a new phase in the phosphate field.

The new phase, $Na_4Ni_5(PO_4)_2(P_2O_7)_2$, was also obtained as a microcrystalline powder by solid-state reaction employing as precursors $Na_4P_2O_7$, α-$Ni_2P_2O_7$, $Ni(NO_3)_2{\cdot}6H_2O$, and $NH_4H_2PO_4$ in molar ratios 1:1:3:2, which were well-mixed and ground in an agate mortar. The mixture was heated at 300 °C in a porcelain crucible to decompose and remove the volatile species. Then, accumulative treatments at 400, 500, 600, 700, and 800 °C for 24 h each were performed. The well-crystallized powder at the end of process was a single phase because the X-ray powder pattern of the bulk product compared well with that calculated from single-crystal data.

Elemental Analysis. Chemical analyses were carried out on an ICP (inductively coupled plasma) apparatus. The determined data (10.1% Na, 31.5% Ni, and 19.7% P) are in good agreement with those calculated (9.9% Na, 31.7% Ni, and 20.1% P).

Single-Crystal X-ray Diffraction. A yellow crystal of prismatic shape and dimensions 0.08 × 0.065 × 0.02 mm was epoxy resin coated and mounted on a Siemens Smart CCD diffractometer equipped with a normal focus 2.4 kW sealed tube X-ray source (Mo Kα radiation, $\lambda = 0.71073$ Å) operating at 40 kV and 30 mA. Data were collected over a hemisphere of reciprocal space by a combination of three sets of exposures. Each set had a different φ angle for the crystal and each exposure of 20 s covered 0.3° in ω. The crystal to detector distance was 6.01 cm. Coverage of the unique set was over 99% complete to at least 23° in θ. Unit cell dimensions were determined by a least-squares fit of 50 reflections with $I > 20\sigma(I)$ and $3° < 2\theta < 46°$. The first 30 frames of data were recollected at the end of the data collection to monitor crystal decay. The intensities were corrected for Lorentz and polarization effects. Scattering factors for neutral atoms and anomalous dispersion corrections for Ni, Na, and P were taken from the *International Tables for Crystallography*.[19] The structure was solved by direct methods and refined in the monoclinic space group $P2_1/c$. Full-matrix least-squares refinement with anisotropic thermal parameters for all the atoms was carried out by minimizing $w(F_o^2 - F_c^2)^2$. The maximum residual electron density was near the Ni atoms. Refinement on F^2 for all reflections, weighted R factors (R_w), and all goodnesses of fit S are based on F^2, while conventional R factors (R) are based on F. R factors based on F^2 are statistically about twice as large as those based on F, and R factors based on all data will be even larger.

All calculations were performed using SMART software for data collection, SAINT[20] for data reduction, SHELXTL to resolve and refine the structure and to prepare material for publication,[21] and ATOMS[22] for molecular graphics.

X-ray Powder Diffraction. X-ray powder pattern of $Na_4Ni_5(PO_4)_2(P_2O_7)_2$ (Figure 1) was taken at room temperature by using a Siemens D-500 diffractometer in the step scan mode, Cu Kα ($\lambda = 1.540598$ Å) radiation, at a step value of 0.02°, measuring for 20 s at each step. The observed reflections were indexed on a monoclinic unit cell using the TREOR program,[23] in very good agreement with the parameters obtained from the single-crystal X-ray study.

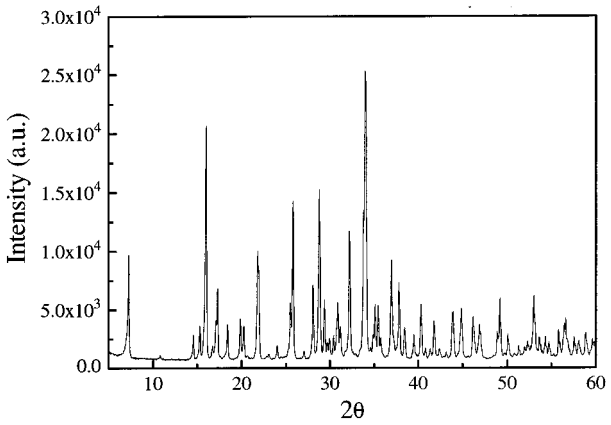

Figure 1. X-ray powder difraction pattern of $Na_4Ni_5(PO_4)_2(P_2O_7)_2$ obtained with monochromatic Cu Kα radiation.

Table 1. Crystal Data and Structure Refinement for 1

empirical formula	$Na_4Ni_5O_{22}P_6$
formula weight	923.32
temperature	296 (2) K
wavelength	0.71073 Å
crystal system	monoclinic
space group	$P2_1/c$
unit cell dimensions	$a = 12.544(2)$ Å, $\alpha = 90°$ $b = 6.596(1)$ Å, $\beta = 103.731(3)°$ $c = 10.572(2)$ Å, $\gamma = 90°$
volume, Z	849.7(3) Å^3, 2
density (calcd)	3.609 g/cm^3
absorption coefficient	6.235 mm^{-1}
$F(000)$	900
crystal size	0.04 mm × 0.08 mm × 0.08 mm
θ range for data collection	3.34°−26.42°
limiting indices	$-14 \le h \le 9$, $-7 \le k \le 7$, $-12 \le l \le 3$
reflections collected	2278
independent reflections	1207 ($R_{int} = 0.0794$)
absorption correction	Sadabs
refinement method	full-matrix least-squares on F^2
data/ restraints/parameters	1207/0/169
goodness-of-fit on F^2	1.000
final R indices [$I > 2\sigma(I)$]	$R_1 = 0.0608$, $wR_2 = 0.1536$
R indices (all data)	$R_1 = 0.0929$, $wR_2 = 0.1693$
largest diff peak and hole	0.969 and −1.063 e Å^{-3}

Magnetic Measurements. Magnetic susceptibility was measured using a Quantum Design MPMS-XL Squid magnetometer operating from 300 to 1.7 K at 500 Oe.

Ionic Conductivity. Impedance measurements were carried out in a frequency response analyzer (Solartron 1174) coupled to an electrochemical interface (Solartron 1286). The frequency range was $1-10^5$ Hz. Pellets of ca. 10 mm diameter and 1.9 mm thickness were prepared by cold pressing the powder sample at 150 MPa. Then, the pellets were sintered at 750 °C for 24 h. The impedance measurements were carried out at steady temperatures on the pellets in still air. The density of the pellets was determined by immersion in ethanol according to the Archimedes method. Platinum electrodes were deposited on the two faces of the pellets by painting with a platinum paste (Engelhard 6082). The painted pellets were heated at 200 °C for 2 h and at 750 °C for 4 h.

Results and Discussion

Crystal Structure. A summary of the fundamental crystal data for $Na_4Ni_5(PO_4)_2(P_2O_7)_2$ is given in Table 1. Final atomic coordinates, and selected bond distances and angles are given in Tables 2 and 3, respectively.

The structure of this new compound is a three-dimensional array which contains three crystallographically independent nickel atoms in normal octahedral

(18) Moring, J.; Kostiner, E. *J. Solid State Chem.* **1986**, *62*, 105.
(19) *International Tables for Crystallography*; Kynoch Press: Birmingham, U.K., 1974; Vol. IV, p 72.
(20) Siemens. SAINT. Data Collection and Procedure. Software for the SMART System. Siemens Analitical X-ray Instruments Inc., Madison, Wisconsin, 1995.
(21) Siemens. SHELXTL. Version 5.0. Siemens Analitical X-ray Instruments Inc., Madison, Wisconsin, 1995.
(22) Dowty, E. ATOMS for Windows 3.1. A Computer Program for Displaying Atomic Structure, 521 Hidden Valley Road, Kingsport, TN 37663, 1995.
(23) Werner, P. E. University of Stockholm, s-106, 91. Stockholm. Sweden 1984.

Table 2. Atomic Coordinates ($\times 10^4$) and Equivalent Isotropic Displacement Parameters ($Å^2 \times 10^3$) for 1

	x	*y*	*z*	*U*(eq)[a]
Ni (1)	6667 (2)	85 (3)	1962 (1)	15 (1)
Ni (2)	10000	0	0	14 (1)
Ni (3)	8672 (2)	2403 (3)	2178 (2)	14 (1)
P (1)	5820 (3)	−2009 (6)	−914 (3)	17 (1)
P (2)	10851 (3)	2367 (5)	2737 (3)	13 (1)
P (3)	7448 (3)	1133 (6)	−671 (3)	14 (1)
Na (1)	8434 (6)	−880 (9)	4581 (5)	31 (2)
Na (2)	6479 (5)	4828 (8)	1343 (5)	18 (1)
O (1)	8399 (7)	−812 (13)	2341 (7)	11 (2)
O (2)	10008 (8)	2141 (13)	1384 (8)	15 (2)
O (3)	6091 (8)	−2004 (15)	563 (8)	20 (3)
O (4)	8470 (8)	5532 (13)	1803 (7)	18 (3)
O (5)	6418 (9)	−1294 (15)	3597 (8)	21 (3)
O (6)	5369 (8)	1964 (13)	1534 (8)	14 (2)
O (7)	10046 (8)	2693 (12)	3658 (7)	11 (2)
O (8)	11654 (8)	446 (13)	483 (8)	14 (2)
O (9)	6296 (8)	129 (15)	−1346 (8)	19 (3)
O (10)	7574 (8)	2236 (14)	3343 (8)	16 (2)
O (11)	7339 (8)	2066 (13)	608 (8)	13 (2)

[a] *U*(eq) is defined as one-third of the trace of the orthogonal U_{ij} tensor.

Table 3. Selected Bond Lengths (Å) and Angles (deg) for 1

Ni(1)−O(6)	2.011(9)	Ni(1)−O(3)	2.025(9)
Ni(1)−O(5)	2.041(9)	Ni(1)−O(10)	2.156(8)
Ni(1)−O(1)	2.195(9)	Ni(1)−O(11)	2.245(10)
Ni(2)−O(2)	2.032(8)	Ni(2)−O(2)[a]	2.032(8)
Ni(2)−O(8)[a]	2.037(9)	Ni(2)−O(8)	2.037(9)
Ni(2)−O(7)[b]	2.090(8)	Ni(2)−O(7)[c]	2.090(8)
Ni(3)−O(7)	2.043(8)	Ni(3)−O(2)	2.052(11)
Ni(3)−O(10)	2.057(11)	Ni(3)−O(11)	2.069(8)
Ni(3)−O(4)	2.105(9)	Ni(3)−O(1)	2.162(9)
Na(1)−O(4)[d]	2.349(9)	Na(1)−O(1)	2.360(10)
Na(1)−O(8)[c]	2.426(11)	Na(1)−O(5)	2.510(12)
Na(1)−O(10)	2.536(10)	Na(1)−O(7)[e]	2.616(9)
Na(1)−O(2)[c]	2.742(13)	Na(2)−O(3)[f]	2.257(11)
Na(2)−O(11)	2.342(11)	Na(2)−O(6)	2.384(11)
Na(2)−O(4)	2.472(12)	Na(2)−O(9)[d]	2.508(11)
Na(2)−O(10)	2.811(10)		
O(6)−Ni(1)−O(3)	97.2(4)	O(6)−Ni(1)−O(5)	100.7(4)
O(3)−Ni(1)−O(5)	102.4(4)	O(6)−Ni(1)−O(10)	90.9(4)
O(3)−Ni(1)−O(10)	169.0(4)	O(5)−Ni(1)−O(10)	83.2(4)
O(6)−Ni(1)−O(1)	157.1(4)	O(3)−Ni(1)−O(1)	96.7(4)
O(5)−Ni(1)−O(1)	94.0(4)	O(10)−Ni(1)−O(1)	73.4(3)
O(6)−Ni(1)−O(11)	84.5(4)	O(3)−Ni(1)−O(11)	93.1(4)
O(5)−Ni(1)−O(11)	162.8(3)	O(10)−Ni(1)−O(11)	80.3(3)
O(1)−Ni(1)−O(11)	76.6(3)	O(2)−Ni(2)−O(2)[a]	179.999(1)
O(2)−Ni(2)−O(8)[a]	96.4(4)	O(2)[a]−Ni(2)−O(8)[a]	83.6(4)
O(2)−Ni(2)−O(8)	83.6(4)	O(2)[a]−Ni(2)−O(8)	96.4(4)
O(8)[a]−Ni(2)−O(8)	180.0	O(2)−Ni(2)−O(7)[b]	89.2(3)
O(2)[a]−Ni(2)−O(7)[b]	90.8(3)	O(8)[a]−Ni(2)−O(7)[b]	97.2(3)
O(8)−Ni(2)−O(7)[b]	82.8(3)	O(2)−Ni(2)−O(7)[c]	90.8(3)
O(2)[a]−Ni(2)−O(7)[c]	89.2(3)	O(8)[a]−Ni(2)−O(7)[c]	82.8(3)
O(8)−Ni(2)−O(7)[c]	97.2(3)	O(7)[b]−Ni(2)−O(7)[c]	180.0
O(7)−Ni(3)−O(2)	72.5(4)	O(7)−Ni(3)−O(10)	96.3(3)
O(2)−Ni(3)−O(10)	165.5(3)	O(7)−Ni(3)−O(11)	176.6(4)
O(2)−Ni(3)−O(11)	104.2(3)	O(10)−Ni(3)−O(11)	86.9(4)
O(7)−Ni(3)−O(4)	95.4(3)	O(2)−Ni(3)−O(4)	94.5(4)
O(10)−Ni(3)−O(4)	95.6(4)	O(11)−Ni(3)−O(4)	85.2(3)
O(7)−Ni(3)−O(1)	98.7(3)	O(2)−Ni(3)−O(1)	96.3(4)
O(10)−Ni(3)−O(1)	76.0(4)	O(11)−Ni(3)−O(1)	81.1(3)
O(4)−Ni(3)−O(1)	164.2(4)	Ni(3)−O(1)−Ni(1)	83.7(3)
Ni(2)−O(2)−Ni(3)	119.2(4)	Ni(3)−O(7)−Ni(2)[g]	115.7(4)
Ni(3)−O(10)−Ni(1)	87.2(3)	Ni(3)−O(11)−Ni(1)	84.6(3)

[a] Symmetry transformations used to generate equivalent atoms: [a] $-x+2, -y, -z$. [b] $x, -y+1/2, z-1/2$. [c] $-x+2, y-1/2, -z+1/2$. [d] $x, -y+1/2, z+1/2$. [e] $-x+2, -y, -z+1$. [f] $x, y+1, z$. [g] $-x+2, y+1/2, -z+1/2$.

coordination, with average Ni−O distances of 2.112(9), 2.053(8), and 2.081(9) Å for Ni(1), Ni(2), and Ni(3), respectively.

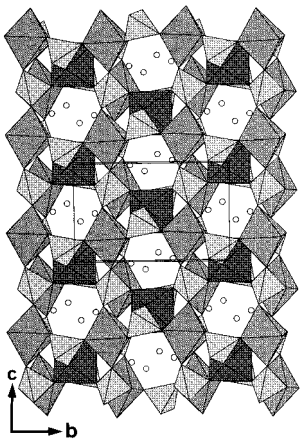

Figure 2. Polyhedral view along [100] direction of $Na_4Ni_5(PO_4)_2(P_2O_7)_2$ showing the channels.

PO_4 and P_2O_7 groups coexist in the new phase. The PO_4 group shows a distorted tetrahedral environment due to the corner- and edge-sharing between the PO_4 unit and MO_6 octahedra, with an average P−O distance P(2)−O = 1.549(9) Å, which is on the same order as those observed before in other phosphates with the same characteristics.[24]

The diphosphate unit is formed, as usual, by two tetrahedra, $P(1)O_4$ and $P(3)O_4$, with the O(9) as bridging oxygen; the P(1)−O(9)−P(3) angle is 125.7(6)°, which is in the range of those found in other diphosphates. This unit shares its six corners with six different NiO_6 octahedra. The $P(1)O_4$ tetrahedron is bonded to three different $Ni(1)O_6$ octahedra, and the $P(3)O_4$ tetrahedron is also joined by three corners to one $Ni(2)O_6$ octahedron and two different $Ni(3)O_6$ octahedra. The P_2O_7 group adopts an alternated conformation as result from their way of connecting to the metal polyhedra, which has been also observed in other phosphates.[25] The $P-O_{bridge}$ distances found in $Na_4Ni_5(PO_4)_2(P_2O_7)_2$ are on the same order as those reported for other similar compounds.[16,26]

There are two crystallographically independent sodium atoms in the structure. Na(1) and Na(2) are in seven- and six-coordination, respectively, the Na−O distances range from 2.257(11) to 2.811(10) Å, and no further oxygens within 3.3 Å have been found. The bond valence calculations give 1.113 and 1.048 for Na(1) and Na(2), respectively.

Despite the complexity of the $Na_4Ni_5(PO_4)_2(P_2O_7)_2$ structure, it can be described in a simple way as built up from $(Ni_5P_2O_{22})_\infty$ blocks, parallel to the *bc* plane (Figure 2). These blocks are crossed by channels running along the *a* direction. Hexagonal tunnels, which are occupied by sodium cations, result from the stacking of rings formed by edges of four octahedra and two tetrahedra.

The projection of $Na_4Ni_5(PO_4)_2(P_2O_7)_2$ along the [010] direction shows how these blocks $(Ni_5P_2O_{22})_\infty$ parallel to the *bc* plane are linked via P(1)−O(9)−P(3) bridges of the diphosphate groups (Figure 3). The three-dimensional structure results from the corner linkage

(24) Bu, X.; Feng, P.; Stucky, G. D. *J. Solid State Chem.* **1997**, *131*, 387.
(25) Gali, S.; Byrappa, K.; Opalakrishna G. S. *Acta Crystallogr. Sect. C.* **1989**, *45*, 1667.
(26) Benmoussa, A.; Borel, M. M.; Grandin, A.; Raveau, B. *J. Solid State Chem.* **1992**, *97*, 314.

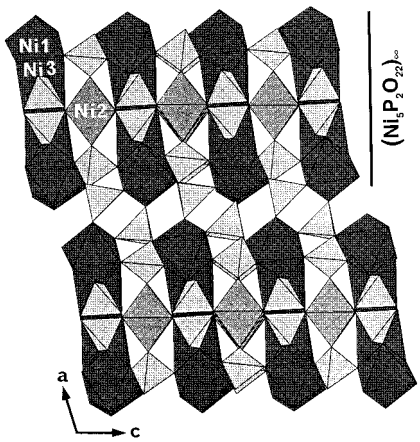

Figure 3. Polyhedral view along [010] direction of the structure of $Na_4Ni_5(PO_4)_2(P_2O_7)_2$.

of two types of unit: parallel stripes of Ni(1)−Ni(3)−Ni(3)−Ni(1)$(PO_4)_2$ = $Ni_4(PO_4)_2$ and Ni(2)$(P_2O_7)_2$ = Ni-$(P_2O_7)_2$.

The structure of this new phase can also be described as constituted by infinite $[Ni_2PO_9]_\infty$ simple chains along the *b* axis (Figure 4) in which one tetrahedron alternates with Ni_2O_9 units (formed by Ni(3)O_6−Ni(1)O_6 octahedra sharing the O(1)−O(10)−O(11) face). These Ni_2O_9 bioctahedral units share corners with two different PO_4 groups through the O(1) and O(4) oxygen atoms.

The "condensation" of two $[Ni_2PO_9]_\infty$ chains by O(2)−O(7) edge-sharing between Ni_2O_9 units and P(2)O_4 tetrahedra leads to the formation of double chains. As a consequence of this arrangement, two types of P−O bonds are found in the monophosphate groups. The P−O distances corresponding to the tetrahedra edge-sharing with octahedra are larger than those for corner-sharing. The angle O(7)−P(2)−O(2), corresponding to edge-shared with Ni_2O_9 units, whose value is 100.6(5)°, is more acute than for an ideal tetrahedron. Besides, extending along the [010] direction (Figure 4), between two consecutive of the above-mentioned chains, there is a row of Ni(2)O_6 octahedra in the way such that the block $(Ni_5P_2O_{22})_\infty$ consists of infinite double chains of composition $(Ni_4P_2O_{22})_\infty$ with nickel rows running in the direction [010] and stacking in the [100] direction.

In Figure 5 two bioctahedral Ni_2O_9 units are joined through their O(7) atoms with one Ni(2)O_6 octahedron. As a result of this arrangement, the subnetwork of nickel atoms can be described as built up from two intersecting zigzag chains of NiO_6 octahedra: extending along [01−1] and [011] directions, both showing a similar sequence—Ni(1)Ni(3)O_9−Ni(2)O_6−Ni(3)Ni(1)-O_9−which intersect at the Ni(2)O_6 octahedra.

It is remarkable that the M_2O_9 units of face-sharing octahedra are also present in $K_{11}V_{15}P_{18}O_{73}$,[26] $V_3P_4SiO_{19}$,[27] $V_4P_6O_{21}$,[28] and $SrFe_3(PO_4)_3(HPO_4)$,[29] and $NiPO_8$ units of an octahedron edge-sharing with a tetrahedron have been previously observed in other nickel phosphates as $Na_4Ni_7(PO_4)_6$,[18] $Ni_3(PO_4)_2{\cdot}H_2O$,[30] and $NH_4NiPO_4H_2O$.[31]

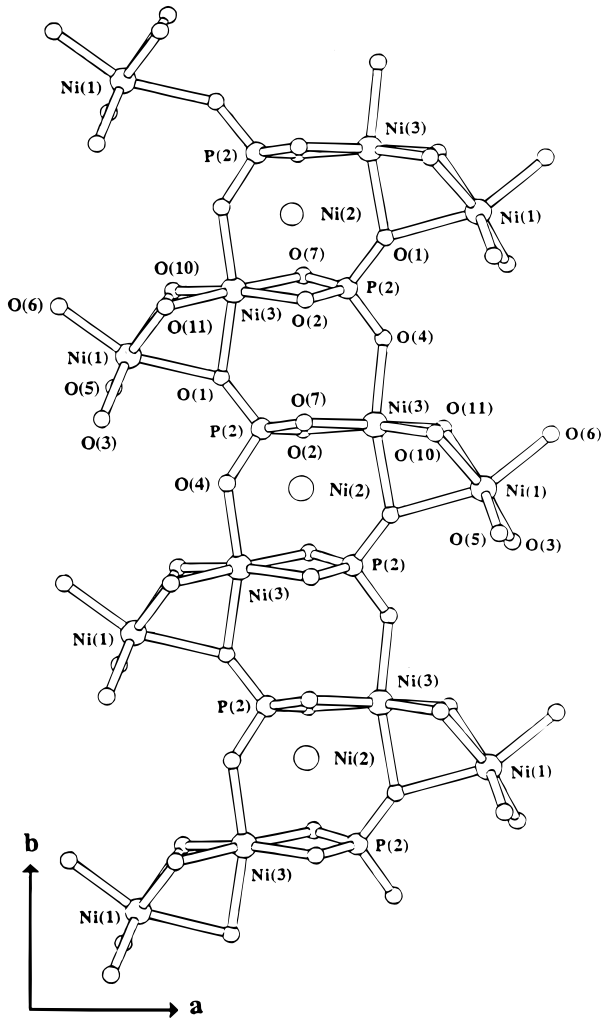

Figure 4. Representation of the double chains $[Ni_2PO_9]_\infty$ showing the corner-, edge-, and face-sharing scheme. Between two double chains a row of octahedral sites occupied by Ni(2) atoms occurs; Ni(2) atoms are without stick-bonds for clarifying.

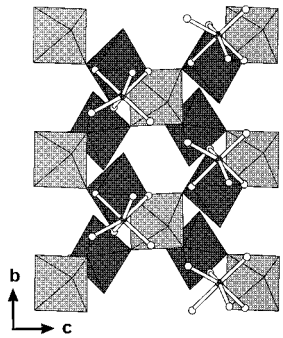

Figure 5. Polyhedral view along [100] direction of the subnetwork of nickel atoms showing the double helix of corner-shared Ni(2) (gray) and Ni(3) (black) octahedra and the face-sharing connection of Ni(1) (sticks) and Ni(3).

It is worth noting that this structure is quite similar to that of $Na_4Co_3(PO_4)_2(P_2O_7)$.[16] Both of them have double chains that are built up from MO_6 octahedra and

(27) Leclaire, A.; Chahboun, H.; Groult, D.; Raveau, B. *J. Solid State Chem.* **1986**, *65*, 168.
(28) Palkina, K. K.; Maksimova, S. Y.; Chitbiskova N. T.; Schlessinger. K.; Ladwig, G. *Z. Anorg. Allg. Chem.* **1985**, *529*, 89.
(29) Lii, K.; Dong, T.; Cheng, Ch.; and Wang, Sue-Lein. *J. Chem. Soc. Dalton Trans.* **1993**, 577.
(30) Fejdi, P.; Poullen, J. F.; Gasperin, M. *Mater. Res. Bull.* **1980**, *103*, 135.
(31) Goñi, A.; Pizarro, J. L.; Lezama, L. M.; Barberis, G. E.; Arriortua, M. I.; Rojo, T. *Mater. Chem.* **1996**, *6* (3), 421.

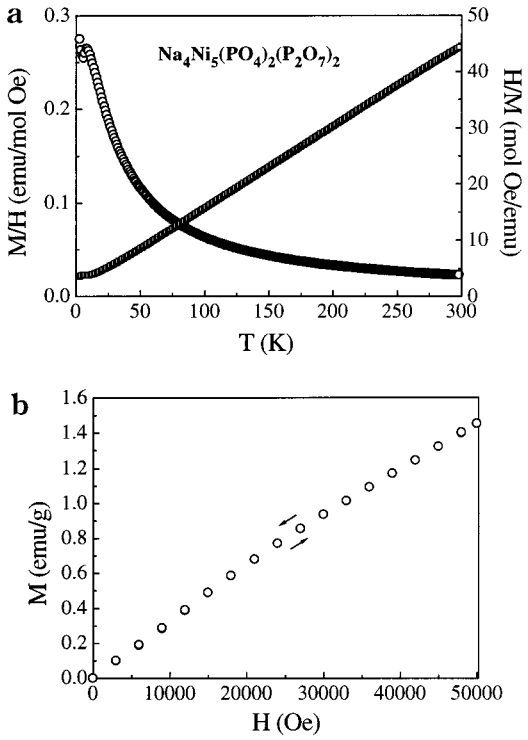

Figure 6. (a) Magnetic susceptibility (M/H, open circles) and inverse magnetic susceptibility (H/M, open squares) plotted as a function of temperature. (b) M vs H plots with the field increased and decreased (see arrows).

PO_4 groups sharing corners. These double chains are formed by simple parallel chains running in the [010] direction. In both compounds there are infinite blocks parallel to the *bc* plane, and interblock linkages are made via diphosphate groups. However, the main difference is the presence of bioctahedral face-sharing units, Ni_2O_9, in the title compound. As a consequence of these units, the framework is less open in this structure, bringing about the formation of tunnels only in the **a** direction, whereas in $Na_4Co_3(PO_4)_2(P_2O_7)$ there are tunnels along the three main crystallographic directions [100], [010], and [001].

Magnetic Properties. The results of magnetic susceptibility measurements in the temperature range from 1.7 to 300 K are plotted in Figure 6a. At lower temperatures the magnetic susceptibility rises to a maximum at 8 K. This behavior should be due to antiferromagnetic ordering of Ni cations. In the range 12−300 K, the inverse magnetic susceptibility follows ($r = 0.9999$) the Curie−Weiss law $\chi^{-1} = 1.46(1) + 0.1443(6)T$, C being 6.93 cm^3K/mol. Using the expression for the Curie constant, the effective moment per Ni^{2+} ion, $\mu = 3.3\ \mu_B$, is obtained, the experimental magnetic moment for Ni(II) compounds[32] being between 2.9 and 3.4 μ_B. A very small increase of χ at temperatures below 4 K is likely due to the presence of a small amount of paramagnetic impurity.

The field dependence on magnetization at 2 K is shown in Figure 6b. In these measurements, the field has been increased and then decreased, as indicated by arrows. A change can be observed in the slope of the curve at approximately 25 000 Oe. The value of extrapolated moment is about 0.1 emu/g, which is obtained by projecting the high-field slope to $H = 0$ in Figure 6b. This result seems to indicate that the $Na_4Ni_5(PO_4)_2(P_2O_7)_2$ phase presents a small metamagnetic field induced behavior at this low temperatures.

Table 4. Selected Angles (deg) Corresponding to NiO_6 Octahedra in a $(Ni_5P_2O_{22})_\infty$ Layers Involving Face- and Corner-Sharing

Ni	angle
M(1)−O(11)−M(3)	84.6(3)[a]
M(1)−O(1)−M(3)	83.7(3)[a]
M(1)−O(10)−M(3)	87.2(3)[a]
M(2)[c]−O(7)−M(3)	115.7(4)[b]
M(3)−O(2)−M(2)	119.2(4)[b]

[a] Angles involving face-sharing. [b] Angles involving corner-sharing. [c] Symmetry code: $-x + 2, y + 1/2, -z + 1/2$.

Considering the structural features exhibited by this compound, different exchange pathways could be a priori involved in the observed magnetic behavior. The subnetwork of Ni polyhedra is two-dimensional from the magnetic point of view. The most effective intralayer interactions occur through −Ni(1)Ni(3)O_9−Ni(2)O_6−Ni(3)Ni(1)O_9− zigzag chains, which are built up from corner- and face-sharing between NiO_6 octahedra, as is shown in Figure 5. Within the layers, there are different magnetic exchange pathways; one of them involves the interactions within the Ni(3)Ni(1)O_9 dimers present in the structure, which could produce a weak ferromagnetic coupling[33] through the three shared oxygens O(1), O(10), and O(11), with intermetallic angles near 90° (Table 4). The Ni(1)−Ni(3) distance is 2.906(3) Å; thus, very weak or no direct interactions could be expected. Another pathway could be considered that implicates the corner-shared NiO_6 octahedra, leading to the superexchange antiferromagnetic interactions via Ni(2)−O−Ni(3), and it seems clear that these interactions govern the exchange despite the weakness of the superexchange angles which appear in Table 4.

It must be noted that, whatever the sign of the interactions between Ni(II) ions through metallic chains, there is no compensation of the spins within the magnetic layer due to the different Wyckoff multiplicity of the three different Ni sites, which is therefore ferrimagnetic. That means that the coupling between two magnetic layers using PO_4 groups must be antiferromagnetic to justify the global antiferromagnetism, as has been observed for other transition metal phosphates.[34,35]

Finally, the weak value of the T_N could be explained by all these facts: weak superchange antiferromagnetic interactions through the corner-shared NiO_6 octahedra, 2D character of the magnetic lattice, and magnetic couplings through the PO_4 groups.

Ionic Conductivity. Impedance measurements were performed on a sintered pellet whose density determined from the Archimedes method was 98% of the density deduced from the crystal structure. Typical impedance plots are shown in Figure 7. At low temperatures (300 °C) an arc and a part of another arc are

(32) Craik, D. *Magnetism: Principles and Applications*; Wiley: New York, 1995.

(33) Hay, P. J.; Thiheault, J. C.; Hoffmann, R. *J. Am. Chem. Soc.* **1975**, *97* (17), 4884.

(34) Lezama, L.; K. Suh, S.; Villenueve, G.; Rojo, T. *Solid State Commun.* **1990**, *76*, 449.

(35) Goñi, A.; Lezama, L.; Barberis, G. E.; Pizarro, J. L.; Arriortua, M. I.; Rojo, T. *J. Magn. Magn. Mater.* **1996**, *164*, 251.

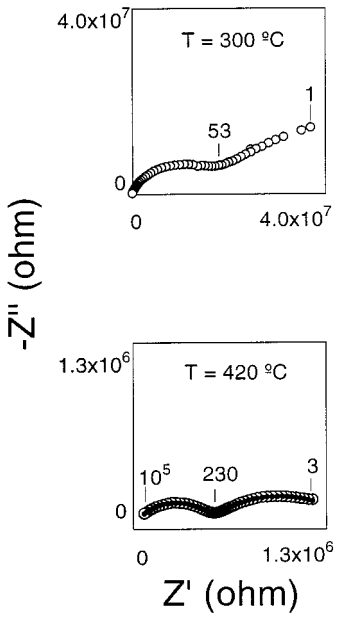

Figure 7. Impedance plots (open circles) obtained at 300 and 420 °C. Selected frequencies (in hertz) are marked. The data at 420 °C are fitted (closed circles) to the expression $Z^* = 1/(1/R_1 + B_1(i\omega)^{n_1} + i\omega C_1) + 1/(1/R_2 + B_2(i\omega)^{n_2} + i\omega C_2)$, where the first and second terms stand for the arcs observed at high and low frequencies, respectively. The fitting parameters are $R_1 = 5.7 \times 10^5$ ohm, $B_1 = 7.28 \times 10^{-10}$, $n_1 = 0.67$, $C_1 = 2.5 \times 10^{-12}$ F, $R_2 = 1.03 \times 10^6$ ohm, $B_2 = 1.5 \times 10^{-7}$, $n_2 = 0.50$, $C_2 = 3 \times 10^{-9}$ F.

observed. At higher temperatures (420 °C) the two arcs are clearly detected: one arc at high frequencies and the other at low frequencies. The impedance plots are well-fitted to the expression $Z^* = 1/(1/R_1 + B_1(i\omega)^{n_1} + i\omega C_1) + 1/(1/R_2 + B_2(i\omega)^{n_2} + i\omega C_2)$, where the first and the second term account for the high- and low-frequency arc, respectively. Each term corresponds to a parallel circuit formed of a resistance, a CPE element, and a capacitor. Both circuits are connected in series. The capacitance deduced from the fit is 3 pF for the high-frequency arc and 3 nF for the low-frequency. These values are on the order of magnitude usually found for the grain-interior and grain-boundary response in sintered ceramic materials.[36,37] In the title compound the high-frequency arc is ascribed to motion of Na^+ ions within the particles and the low-frequency one to motion of these ions through boundaries of neighboring particles. From the fit of the impedance plots we have also obtained the resistance of the two arcs, and the overall resistance of the pellet. Then, the conductivity values are calculated as usual. Another fit of the impedance data was tried through the expression $Z^* = 1/(1/R_1 + B_1(i\omega)^{n_1}) + 1/(1/R_2 + B_2(i\omega)^{n_2})$. Although the values of B_1, B_2, n_1, and n_2 are slightly different from those obtained with the other expression, the values of R_1 and R_2 deduced from both fittings are quite close. When the pellets are heated at higher temperatures (500−700 °C), the arcs disappear progressively, and above 700 °C only an inclined spike is detected (not shown). The spike is due to blocking of the Na^+ ions at the electrode surface.

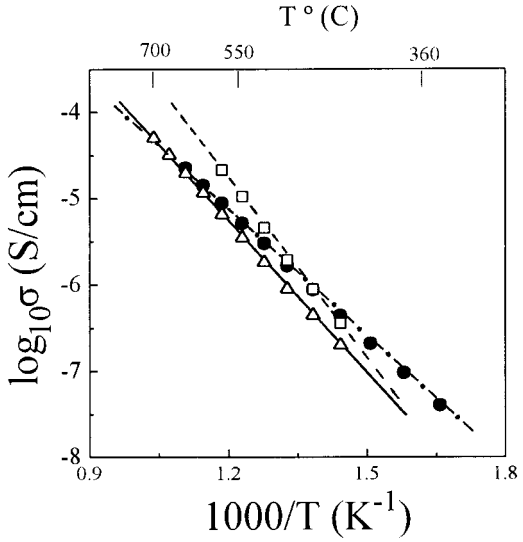

Figure 8. Temperature dependence of the conductivity in an Arrehenius plot. Closed circles, open squares, and open triangles stand for the grain-interior, grain-boundary, and overall conductivity, respectively.

Table 5. Activation Energy (E_σ) and Pre-Exponential Factor (σ_0) for the Arrhenius Plots of Figure 8

$Na_4Ni_5(PO_4)_2(P_2O_7)_2$	E_σ (eV)	σ_0 (S cm^{-1})
grain interior (●)	0.99	8
grain boundary (□)	1.37	3428
overall (△)	1.18	77

Plots of conductivity (log σ) against inverse temperature (1000/T) are shown in Figure 8. The grain-interior and overall conductivity are represented by closed circles and open triangles, respectively. The grain-boundary conductivity (open squares) is also shown, although the grain-boundary surface area is unknown and, hence, the grain-boundary conductivity is an apparent conductivity. It is observed that the overall conductivity is close to the grain-interior one at high temperatures (T > 550 °C), indicating that the overall conductivity is dominated by the grain-interior contribution. However, at temperatures below 550 °C the overall conductivity is lower than the grain-interior one, as a consequence of the negative contribution of the grain-boundary conductivity, this contribution becomes more significant as the sample temperature decreases. All the conductivity data are well-fitted to Arrhenius expressions [$\sigma = \sigma_0 \exp(-E_\sigma/kT)$, where σ_0 is a preexponential factor, E_σ the activation energy, and k the Boltzmann constant]. The E_σ and σ_0 values deduced from the three fits are outlined in Table 5.

The grain-interior conductivity ($\sigma = 2.8 \times 10^{-6}$ S cm^{-1} at 500 °C) is lower and the activation (0.99 eV) higher as compared with the values reported for good sodium ion conductors such as Nasicon, related Nasicon compounds, and β-alumina.[38−42] Although the presence of hexagonal channels in the framework, along the [100]

(36) Bruce, P. G.; West, A. R. *J. Electrochem. Soc.* **1983**, *130*, 662.
(37) Bonano, N.; Slotwiski, R. K.; Steele, B. C. H.; Butler, E. P. *J. Mater. Sci.* **1984**, *19*, 785.
(38) Hong, H. Y. P. *Mater. Res. Bull.* **1976**, *11*, 173.
(39) Goodenough, J. B.; Hong, H. Y. P.; Kafalas, J. A. *Ibid.* **1976**, *11*, 203.
(40) Winand, J. M.; Rulmont, A.; Tarte, P. *J. Mater. Sci.* **1990**, *25*, 4008.
(41) Collongues, R.; Kahn, A.; Michel, D. *Annu. Rev. Mater. Sci.* **1979**, *9*, 123.
(42) Martínez-Juarez, A.; Pecharromán, C.; Iglesias, J. E.; Rojo, J. M. *J. Phys. Chem. B* **1998**, *102*, 372.

direction, allows motion of the Na^+ ions in this direction, the ions move with difficulty, as indicated by the high activation energy.

Acknowledgment. This work was supported by the Spanish CICYT under Projects No. PB97-1200 and MAT 98-1735-E. We thank the staff of C.A.I de Espectroscopia de Plasma, UCM, for chemical analysis, Dr. R. Saez-Puche for the magnetic measurements, and Dr. I. Rasines and Dr. A. Monje for fruitful comments.

Supporting Information Available: Observed and calculated structure factors anisotropic displacement parameters, and bond lengths + angles for **1**. This material is available free of charge via the Internet at http://pubs/acs/org.

CM981105S